

Analytical and Monte-Carlo modeling of Multi-Parallel Slit and Knife-Edge Slit Prompt Gamma Cameras

Brent F. B. Huisman^{1,2}, É. Testa², D. Dauvergne³, J. M. Létang¹, and D. Sarrut¹

¹ CREATIS, Université de Lyon; CNRS UMR5220; INSERM U1206; INSA-Lyon; Université Lyon 1; Centre Léon Bérard, Lyon, France

² IPNL, Université de Lyon; CNRS/IN2P3 UMR5822; Université Lyon 1 Lyon, France

³ Laboratoire de Physique Subatomique et de Cosmologie, CNRS/IN2P3, Grenoble, France

E-mail: e.testa@ipnl.in2p3.fr

August 21, 2019

Abstract

Purpose:

Materials and Methods:

Results:

Conclusion:

Contents

1	Introduction	3
2	Materials and Methods	3
2.1	Analytical model for spatial resolution and detection efficiency	3
2.1.1	Spatial resolution	4
2.1.2	Detection efficiency	5
2.2	Monte Carlo simulations	7
2.2.1	Simulation tool	7
2.2.2	PG Camera modeling	7
2.2.3	Background modeling	9
2.2.4	Beam and target	9
2.2.5	AMV-specific alterations to setup	9
2.3	Figures of merit	9
2.3.1	Analytical Model Verification	9
2.3.2	Prototype Comparison	10
3	Results	10
3.1	Analytical Model Verification	10
3.2	Prototype Comparison	11
3.2.1	PG profiles	11
3.2.2	FRP	12
4	Discussion	12
5	Conclusion	13
6	Acknowledgements	13

A	Fall-off position and width estimation procedure	14
A.1	Fall-off position estimation procedure	14
A.2	Fall-off width estimation procedure	14
B	Verification of the cameras	16

1 Introduction

The well-defined range of particles in matter is the main reason they are used in cancer treatment today. Unfortunately we are not able to take full advantage of this property, because of treatment uncertainties, e.g. uncertainties in patient positioning, changes of patient anatomy between treatment fractions and uncertainties in the Hounsfield unit to particle stopping power conversion (Paganetti, 2012). Often, medical practice leads to the use of several irradiation fields to ensure robust treatment planning at the expense of larger doses in healthy tissue in respect to ideal treatment with single irradiation field. Moreover margins around the tumor are added, greatly reducing the potential benefits of particle treatment (Knopf and Lomax, 2013). Ion-range verification could permit more precise planning which could take maximum advantage of the steep Bragg peak (BP) fall-off and reduce damage to tissues surrounding the tumor. A promising modality to perform this verification consists in detecting prompt gammas (PGs), a natural byproduct in particle treatments (Krimmer et al., 2017b; Parodi and Polf, 2018). Various modalities are currently under investigation and can be classified in two categories: imaging devices using either mechanical or electronical collimation (respectively collimated (Min et al., 2012; Perali et al., 2014; Pinto et al., 2014) and Compton cameras (Krimmer, 2015; Kurosawa et al., 2012; Llosá et al., 2016; Polf et al., 2015; Thirolf et al., 2016)) and non-imaging devices such as Prompt Gamma Spectroscopy (PGS) (Hueso-González et al., 2016), Prompt Gamma Timing (PGT) (Pausch et al., 2016) and Prompt Gamma Peak Integral (PGPI) (Krimmer et al., 2017a). Regarding cameras using mechanical collimators, two types of designs have been considered: Multi-Parallel Slit (MPS) and Knife-Edge Slit (KES). The latter has been chosen by the IBA group to build their prototype that has been tested during the treatment of a patient at OncoRay in Dresden, Germany. Both types of collimators provide part or the whole of the 1D PG profile along the beam direction.

To date three publications (Lin et al., 2017; Park et al., 2017; Smeets et al., 2016) have attempted to compare these two types of collimators. In the three studies the same KES design has been chosen (the one of the IBA group (Perali et al., 2014)) while various geometries have been used for the MPS design: a modified design from Pinto et al. (2014) in (Smeets et al., 2016), the one of Gueth et al. (2013) in (Lin et al., 2017) and a specific “optimized” system in (Park et al., 2017). It is worth to note that the authors of the latter publication justified the need for a complementary study by the fact that the MPS geometries used in Lin et al. (2017); Smeets et al. (2016) were not “optimized”. Unfortunately the fact that the optimizations of KES and MPS designs were not performed according the same figures of merit leads to another bias in the comparison. Actually from a general point of view the design of any collimated device is a compromise between detection efficiency and spatial resolution. While collimator features have been extensively investigated in the context of nuclear imaging (Gunter, 2004), no theoretical considerations have been proposed for the specific 1D collimation systems developed in the context of ion-range verification during hadrontherapy.

Therefore the first objective of the present article is to present an analytical model based on geometric considerations that allows for a theoretical estimation of the detection efficiency and spatial resolution, for both MPS and KES. The intrinsic features of MPS and KES collimators are then derived and the model is validated by means of Monte Carlo (MC) simulations. In light of the predictions of this analytical model, the PG prototypes developed by the CLaRyS collaboration and the IBA group are compared and their performances are assessed in terms of detection efficiency, spatial resolution and fall-off retrieval precision thanks to MC simulations.

2 Materials and Methods

2.1 Analytical model for spatial resolution and detection efficiency

In order to compare performance of different camera types and configurations, we derive an analytical model that predict camera performance, namely spatial resolution and detection efficiency, for both MPS KES collimators. Such models allow to estimate variation in performance according to variation in geometrical parameters assuming in most cases full gamma absorption both in the collimator and the absorber. Such assumptions are equivalent to consider respectively a perfect collimator and a perfect gamma detection (full absorption on absorber entrance surface).

Figure 1 presents the schemes of the MPS and KES cameras gathering of the geometrical parameters defined in Table 1.

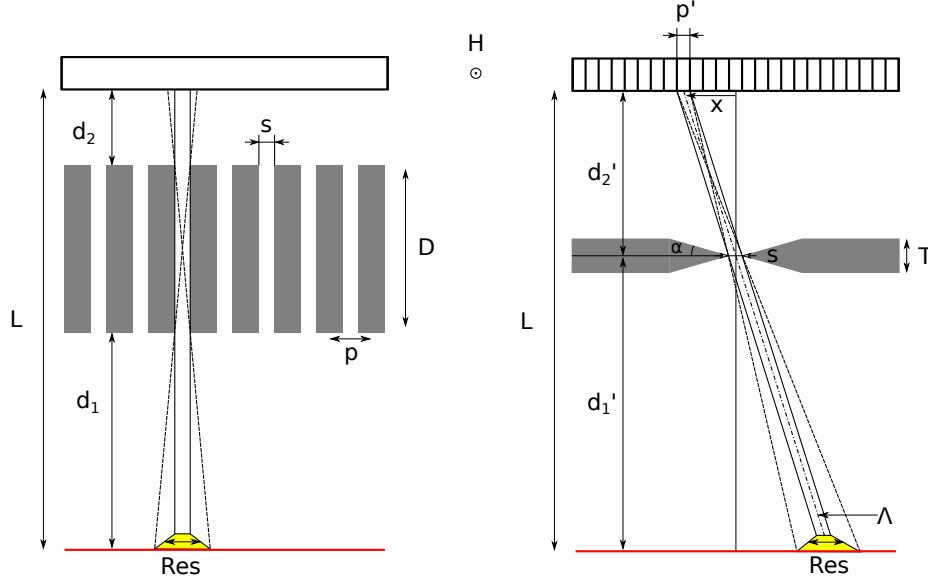


Figure 1: Schemes of the Multi-Parallel Slit (MPS) and the Knife-Edge Slit (KES) cameras. The definition of the various parameters is given in Table 1. The red line corresponds to a linear source perpendicular to the slit camera planes. Λ is the distance between the source point and the gamma detector in the KES.

	MPS	KES
Source-collimator distance	d_1	d'_1
Collimator-absorber distance	d_2	d'_2
Source-absorber distance	$L = d_1 + D + d_2$	$L = d'_1 + d'_2$
Collimator thickness	D	T
Camera pitch	p	p'
Knife-edge slit angle	\emptyset	α
Slit width	s	

Table 1: Geometrical parameters of the MPS and KES cameras. One can also define the fill factor f of the MPS collimator: $f = (p - s)/p$ (ratio between the septa width and the pitch).

2.1.1 Spatial resolution

From a geometrical point of view, the spatial resolution is characterized by the *detector unit field of view*, denoted Res . This is the portion of the source that can be seen through a single camera unit: a single slit for the MPS and a single detector unit for the KES. The probability of a photon emitted at a given point along a linear source perpendicular to the slit plane to reach this detector unit can be described as an isosceles trapezoid whose width of the top segment corresponds to the slit width while the width of the base segment is equal to the sum of the slit width and the penumbra. We defined Res as the FWHM of this trapezoid, see eq 1 and 2.

$$\text{Res}^{\text{MPS}} = s \left(1 + \frac{d_1}{D} \right) = p(1 - f) \frac{D + d_1}{D} \quad (1)$$

$$\text{Res}^{\text{KES}} = s \left(1 + \frac{d'_1}{d'_2} \right) = \frac{sL}{d'_2} \quad (2)$$

If collimator transparency is neglected, Res is fully defined by geometrical parameters, in particular

the slit width s . However, prompt gamma have high penetration capability that can not be neglected in the case of KES where the collimator depth is very small in the region of the knife edge around the slit. Indeed, we define the *Effective Slit Opening* s_e that can be used in the evaluation of the field of view and the efficiency in place of the geometrical slit width. Metzler and Accorsi (2005) proposed a method to estimate the effective slit width, specifically to calculate the spatial resolution accurately. The proposed expressions were based on one-dimensional cuts through the pinhole geometry and can be applied directly to a knife-edge geometry without modification. Their approach is for a point source and dependent on the location of the source within the Res. For a source in the center, it simplifies to eq. 3 with μ the linear attenuation length of the collimator material.

$$s_e = s + \frac{\ln 2}{\mu \tan \alpha} \quad (3)$$

$$\text{Res}^{\text{KES}} = s_e \left(1 + \frac{d'_1}{d'_2} \right) = \frac{s_e L}{d'_2} \quad (4)$$

Hence, eq. 1 and eq. 4 represent the spatial resolution of the MPS and KES camera systems according to simple geometrical and gamma attenuation parameters (collimator distances, angle and collimator linear attenuation length). The spatial resolution is expressed in millimeters.

2.1.2 Detection efficiency

The probability that a gamma reaches a given detector unit is described by the solid angle Ω_D of the detector unit in respect to the gamma emission point.

For MPS, the solid angle is composed of the azimuthal angle and the polar angle. With small angle approximation, it is described by eq. 5. Note that this is true only when Ω_D is limited by the slit width, i.e. the absorber size and the distances (e.g. L and D) are such that all photons that cross the collimator impinge on detector material.

For KES, the solid angle under which a point of the source sees a detector unit depends on the location of the point source, x , since the distance between source and detector changes significantly over the field of view of the camera. We consider the solid angle for a point of the source that is within the central part of the field of view of the crystal at location x on the detector plane (the origin of the detector plane facing the center of the slit). Under small angle approximation, the solid angle is given by eq. 6.

$$\Omega_D^{\text{MPS}} = \frac{H}{L} \frac{s}{D + d_1} \quad (5)$$

$$\Omega_D^{\text{KES}} = \frac{H L p'}{\Lambda^3(x)} = \frac{H p'}{L^2 \left(1 + \frac{x^2}{d_2^2} \right)^{3/2}} \quad (6)$$

with Λ the distance between the source point and the crystal in the KES.

Since we are interested in extended gamma emission source, let us consider now a linear source in front the cameras (red lines in Figure 1). In this case, the camera detection efficiency is determined not only by the point source detection efficiency (PSDE) characterized by Ω_D but also by the fraction of the source seen by the camera (the FOV factor) $f_{\text{FOV}} = \frac{\text{Res}}{p}$ where p is the pitch of the camera. It is in principle larger than 1 since cameras are usually designed to see all the source without any hidden regions.

Hence the detection efficiency of a detector unit (Eff) and therefore the detection efficiency of the whole camera located in front a linear source perpendicular to the camera plane can be expressed as:

$$\text{Eff} = \text{PSDE} \times f_{\text{FOV}} \quad (7)$$

with PSDE the detection efficiency for a point-like source that sees a detector through the slit, and $f_{\text{FOV}} = \frac{\text{Res}}{p}$ the FOV factor. The detection efficiency of MPS and KES are given by eq. 8 and 9, respectively.

$$\begin{aligned}
\text{Eff}^{\text{MPS}} &= \frac{\Omega_D^{\text{MPS}} \text{Res}^{\text{MPS}}}{4\pi p} \\
&= \frac{1}{4\pi} \frac{H}{L} \frac{s}{D+d_1} p(1-f) \frac{D+d_1}{D} \frac{1}{p} \\
&= \frac{Hs(1-f)^2}{4\pi LD}
\end{aligned} \tag{8}$$

$$\begin{aligned}
\text{Eff}^{\text{KES}} &= \frac{\Omega_D^{\text{KES}} \text{Res}^{\text{KES}}}{4\pi p'} \\
&= \frac{s_e H}{4\pi d'_2 L} \frac{1}{\left(1 + \frac{x^2}{d'^2_2}\right)^{3/2}}
\end{aligned} \tag{9}$$

The formulas of detection efficiency and spatial resolution of MPS and KES cameras are gathered in table 2. The most striking feature of these formulas is their similarities. Indeed with the same source-collimator distances ($d_1 = d'_1$) and if the MPS collimator thickness is equal to the KES collimator-absorber distance ($D = d'_2$) then the effective slit width of the KES (s_e) is equal to s considering perfect collimators with infinite absorption capacity. In this conditions MPS and KES have therefore the same spatial resolution s .

	MPS	KES
Effective slit width (s_e)	s	$s + \frac{\ln(2)}{\mu \tan(\alpha)}$
Spatial resolution (Res)	$s \left(1 + \frac{d_1}{D}\right)$	$s_e \left(1 + \frac{d'_1}{d'_2}\right)$
Detection efficiency (Eff)	$\frac{Hs}{4\pi LD} (1-f)$	$\frac{Hs_e}{4\pi L d'_2} \left(1 + \frac{x^2}{d'^2_2}\right)^{-3/2}$
Collimator effective thickness (T_e)	$D \times f$	T

Table 2: MPS and KES detection efficiencies and spatial resolutions from the analytical model. The parameters of the cameras are defined in figure 1. μ is the linear attenuation length of the collimator material.

Regarding the detection efficiency, since the filling factor f of the MPS can be decreased down to zero considering perfect collimators, the MPS and KES detection efficiencies are strictly equivalent in the central part of the cameras ($x = 0$) (with still $d_1 = d'_1$ and $D = d'_2$).

The MPS and KES designs have therefore the same spatial resolutions and detection efficiencies assuming perfect collimators. The main deviations between the actual MPS and KES performances are the following:

- the partial transparency of the collimators leads to:
 - an effective slit width of KES larger than the one of the MPS ($s_e > s$). In the case of the KES prototype of the IBA group, the term accounting for collimator transparency $\left(\frac{\ln(2)}{\mu \tan(\alpha)}\right)$ is about 5 mm (with $\mu \sim 8 \times 10^{-1} \text{ cm}^{-1}$ in the 3-6 MeV range and $\alpha = 63^\circ$) meaning that the effective slit s_e is about twice the actual slit width s .
 - an actual fill factor that cannot be neglected: in the case of the MPS prototype of the CLaRyS collaboration it can be adjusted but a standard value is 0.4 leading to an actual detection efficiency about half the one of the perfect MPS collimator with $f = 0$.
- the KES design intrinsically leads to a detection efficiency that decreases when the source moves away from the center of the camera while the MPS detection efficiency remains constant over the whole camera field of view.

It is worth to note that the collimator transparency leads to an increase of the KES spatial resolution (Res) and a decrease of the MPS detection efficiency (Eff) with similar amplitudes (factor of 2). Since both Res and Eff are proportional to the slit width s one can expect that a KES and MPS designs should have very close actual performances if the KES slit width corresponds to the half of the MPS slit width.

For illustration purpose, Figure 2 shows the analytical model predictions for the MPS and KES designs compared in (Lin et al., 2017; Park et al., 2017; Smeets et al., 2016). We can observe the compromise between detection efficiency and spatial resolution: the designs chosen in these comparisons lead to Eff^{KES} and Res^{KES} larger than MPS ones by factors ranging from ~ 3 to ~ 7 .

Figure to be improved if we think it is interesting

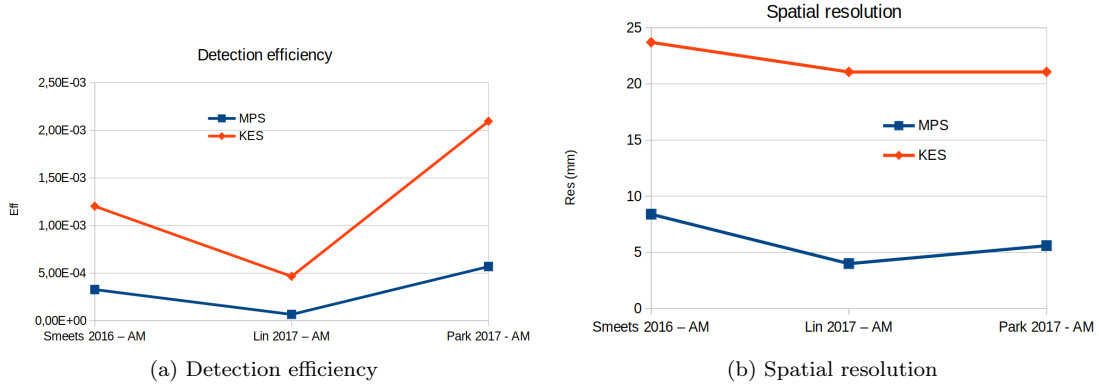


Figure 2: Analytical model predictions for the MPS and KES designs compared in (Lin et al., 2017; Park et al., 2017; Smeets et al., 2016).

2.2 Monte Carlo simulations

2.2.1 Simulation tool

Imaging paradigms such as PG detection are evaluated against experiments, and often also with Monte Carlo (MC) simulations (Golnik et al., 2014; Gueth et al., 2013; Janssen et al., 2014; Moteabbed et al., 2011; Robert et al., 2013). For rarely occurring processes such as PG simulation, convergence to the model of the truth to within acceptable statistical error can be slow. Therefore we used in this study the vpgTLE variance reduction method described in Huisman et al. (2016). vpgTLE is a two stage process, where firstly a PG yield distribution image is estimated, which in the second stage is used as a PG source with which can be investigated. Gate 7.2 (Sarrut et al., 2014) with Geant 4.10.02 and the QGSP_BIC_HP_EMY physics list, commonly used for PG studies, are used in this analysis. Thanks to vpgTLE, simulations for about 10^9 protons (about 6×10^8 photons) took 1-2 hours on a single core of an Intel(R) Core(TM) i7-3740QM.

2.2.2 PG Camera modeling

The two following MPS and KES prototypes (illustrated in fig. 3) were chosen:

- the CLaRyS multi-parallel-slit (MPS) camera, Case 1 (Pinto et al., 2014)
This camera intends to measure the whole PG profile to control ion-ranges in the patient with a field of view (FoV) of 300 mm. It consists of a bismuth germanium oxide (BGO) absorber and a tungsten alloy collimator. It makes use of ToF selection to reduce the neutron background. In the optimization carried out by Pinto et al. (2014), parameters such as collimator pitch, axis-to-collimator and axis-to-detector were varied, and their impacts evaluated in terms of fall-off retrieval precision (FRP) and spatial resolution (sharpness of the fall-off region). Here, configuration 1 (with relaxed constraints on spatial resolution) was chosen for its optimal FRP performance.
- the IBA knife-edge slit (KES) camera (Perali et al., 2014; Sterpin et al., 2015)
The purpose of this camera consists of verifying the BP position with a FoV of 100 mm. It consists of a Cerium doped Lutetium based (LYSO) absorber and a tungsten alloy collimator. Richter

et al. (2016) provides the first clinically obtained results. At this time, no other camera has been subjected to clinical tests, which is why we consider this prototype a benchmark.

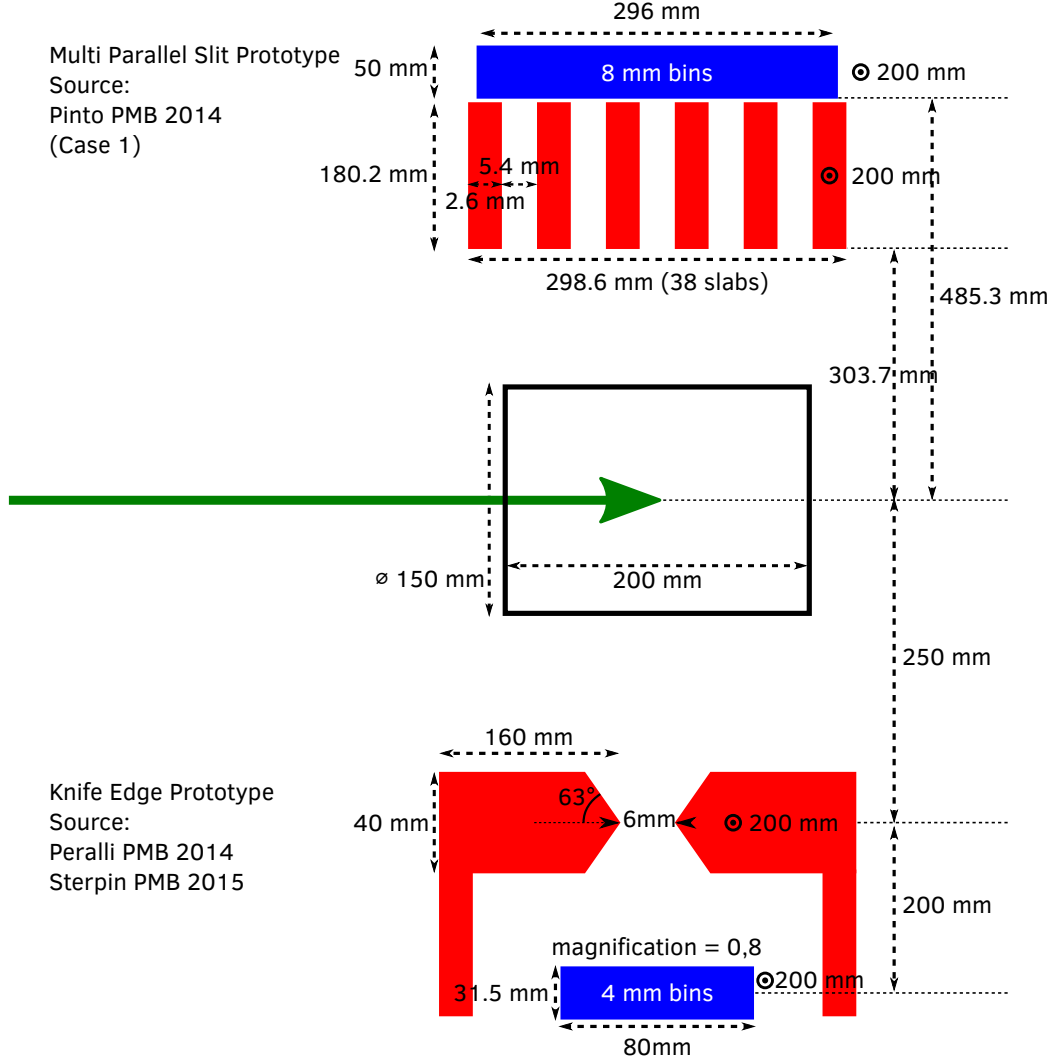


Figure 3: Schematic presentation of the two PG cameras considered in this study. The green arrow represents the proton beam. In red the collimation elements and in blue detection elements. The dimensions were taken from Pinto et al. (2014) and Perali et al. (2014); Sterpin et al. (2015). Note that the two cameras have an identical detector height (\odot symbol), the two cameras were positioned at an identical location above the head during all simulations, and that here they are not drawn to scale.

Regarding background ToF selection, for the IBA C230 accelerator with a period of 10 ns, Pinto et al. (2014) chose a window of 4 ns around the PG maximum, based on experimental ToF spectra. This means that about 60% of the noise could be removed. For the KES prototype ToF is not used, leading to a higher background, as is evident when one compares the backgrounds as published in the two publications. A second difference is the energy selection window. The IBA group employ a 3-6 MeV window, whereas the CLaRyS collaboration produced their optimization with a 1-8 MeV window. We will compare each camera with their published properties, that is to say: a 1-8 MeV window and ToF for MPS and a 3-6 MeV window without ToF for KES.

Both PG camera prototypes have different photodetectors and different detector electronics. In this study, these differences are not implemented. Instead, the method as described in Gueth et al. (2013) was used to obtain the interaction point of an impinging photon. If the integrated energy deposited in a

crystal lies in the acceptable energy and ToF window, the event is recorded. The position of the event in the crystal is considered as the energy weighed barycenter of all interactions in the crystal, plus a random value taken from a 5mm FWHM Gaussian to simulate the electronics and the detector resolution.

2.2.3 Background modeling

Background estimation in PG simulation is a difficult and largely unsolved issue (Huisman et al., 2016; Perali et al., 2014; Pinto et al., 2014; Sterpin et al., 2015). Simulations would ideally include beam nozzle and whole room modeling, but these are habitually omitted. ToF selection techniques can improve the signal-to-noise ratio (SNR) (Roellinghoff et al., 2014; Testa et al., 2008), but then depend on the proper simulation of the beam accelerator time structure. As noted in Huisman et al. (2016), no validation for background in PG simulations has been performed at this time. In this study, the stable time structure of current generation cyclotrons was assumed, in which the neutron background is largely constant.

Estimates of background counts in the detector are taken from Perali et al. (2014); Pinto et al. (2014), which are both based on measured data:

- MPS: Pinto et al. (2014) fig. 9: $1 \cdot 10^3 \pm 1 \cdot 10^2$ per $4 \cdot 10^9$ primary protons per 8 mm bin
Converted to per primary proton: $2.5 \cdot 10^{-7} \pm 0.25 \cdot 10^{-7}$
- KES: Perali et al. (2014) fig. 11: $5 \cdot 10^{-7} \pm 0.5 \cdot 10^{-7}$ per primary proton per 4 mm bin

Per unit of bin length, the background yield of the MPS with ToF is therefore 4 times as low as the background seen with the KES. In the context of the fair comparison, for the KES camera the background with ToF can be obtained by multiplying the background with the same $\frac{4ns}{10ns} = 0.4$ fraction as with the MPS. For the AMV, the background will be left out, as only PG detection was modelled.

2.2.4 Beam and target

We use the test-case presented in Perali et al. (2014) as the KES detector properties such as background were published for that scenario, again in order to remove any doubt that a difference in camera performance could be due to a difference in implementation or setup. A 160 MeV mono-energetic proton beam is shot into a cylindrical PMMA phantom (length 30 cm, radius 15 cm). Employing the batch method we realize 50 simulations for each experiment.

2.2.5 AMV-specific alterations to setup

In the case of simulation for analytical model verifications, we use identical absorbers for both prototypes, namely the absorber of the KES prototype and we apply the same energy and TOF selection: the same energy selection ($E > 1$ MeV) and the same TOF selection (no TOF selection). Since AMV deals with gamma detection, no background modeling is applied in this AMV-specific setup.

Table 3 gives an overview of the main cameras parameters used for AMV and prototypes comparison.

To be modified according to Table 3 which is up to date.

2.3 Figures of merit

2.3.1 Analytical Model Verification

The comparison of the analytical model with Monte Carlo simulations will be performed on the two features predicted by the model, namely the detection efficiency and the spatial resolution

Detection efficiency The detection efficiency can be defined as the ratio of the mean number of detected gammas over the number of emitted gammas for camera units seeing the PG profile.

Spatial resolution Let us define the width of the PG profile fall-off (FOW) as the FWHM of the peak resulting from the computation of the PG profile first derivative.

The FOW of the detected PG profiles can be obtained in principle using summation in quadrature of the FOW of PG emission profiles (FOW_e) and the spatial resolution of the cameras (Res). Since $FOW_e \sim 5$ mm according to simulated profiles (Krimmer et al., 2017b) and Res of the MPS and KES prototypes ranges from 10 to 20 mm (Pinto et al., 2014; Smeets et al., 2012), we can consider that FOW is mainly determined by the camera spatial resolution (Res).

		Analytical model verification (AMV)	Prototypes comparison (PC)
Absorber	MPS	Perfect or like PC	BGO
	KES		LYSO
Collimator		Perfect or like PC	Tungsten alloy
Energy selection	MPS	>1 MeV	>1 MeV
	KES		3–6 MeV
TOF selection	MPS	no TOF	TOF
	KES		no TOF
Background modeling		No modeling	Experimental data based modeling
Target		No	Cylindrical PMMA phantom
Beam		160 MeV proton	

Table 3: Summary of the main cameras parameters used for AMV and prototypes comparison. In the case of AMV, the gamma source corresponds to the PGs emitted during the PMMA phantom irradiation with 160 MeV proton beam (first stage of the simulation tool, see section 2.2.1). However the target has been removed in the second stage of the simulation tool (PG detection) to avoid any attenuation and allow for a direct comparison of the detection efficiency with the AM predictions.

2.3.2 Prototype Comparison

In the comparison of the nominal (unequalized) prototypes, we also take a look at the figures of merit (summarized in table 4). In addition, because of its clinical relevance, the fall-off retrieval precision (*FRP*) will be determined. The FRP is the standard deviation of the FOP, which is obtained by way of the batch method. Each of these can then be examined as function of the energy and ToF selections.

Table 4 presents the figures of merit used for the analytical model verification and the prototypes comparison.

	Analytical	MC
Detection efficiency	Eff	Eff _{MC}
Spatial resolution	Res	FOW

Table 4: Figures of merit for the analytical model verification. FOW: Fall-off width.

3 Results

3.1 Analytical Model Verification

Figures 4: PG profiles obtained with MPS and KES with perfect absorber, the same energy $E > 1$ MeV and no TOF selection.

Table 5 compares the detection efficiency and the spatial resolution obtained from the analytical model and Monte Carlo simulations. Since the model does not explicitly deal with collimator transparency or absorber efficiency, we compare the AM to a Monte Carlo simulation with perfect absorber and collimator. Because such conditions are unphysical, results with a physical collimator and physical absorber are shown for the spatial resolution and detection efficiency respectively.

When we make the collimator perfectly absorbing (any tracks entering the collimator material are killed), we observe the KES's effective slit width in action: the transmission through the collimator creating a wider s_e is gone and we see the FOW decrease between 40 and 100%. This is roughly in line with the calculated s_e : **ETIENNE?** Surprisingly the FOW of the KES approaches the theoretical value nearly, while the MPS is still a few millimeters worse than calculated.

update of the figure with the parameters defined in Table 3 (column AMV with perfect collimator and absorber) and the same layout as Figure 5.

Table 5 1) We have in principle 4 combinations with real/perfect collimator and real/perfect absorber. I propose to use only two configuration for each measurement (Res and Eff). Res: real/perfect collimator with perfect absorber to see the influence of collimator transparency on Res. Eff:

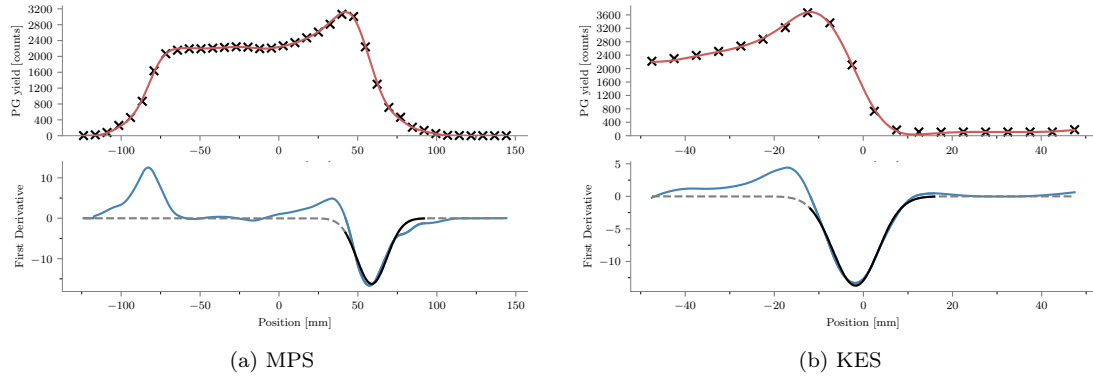


Figure 4: MPS and KES comparisons with perfect absorber and the same energy ($E > 1$ MeV) and no TOF selection.

		MPS		KES		KES/MPS	
		AM	MC	AM	MC	AM	MC
Res	Physical collimator		17.2 mm		19.3 mm		
	Perfect detector	14.5 mm	22.5 mm	13.5 mm	12.0 mm		
Eff	Physical absorber		$3.40 \cdot 10^{-4}$		$3.48 \cdot 10^{-4}$		1.02
	Perfect detector	$6.66 \cdot 10^{-4}$	$6.49 \cdot 10^{-4}$	$1.06 \cdot 10^{-3}$	$9.74 \cdot 10^{-4}$	1.59	1.50

Table 5: MPS and KES detection efficiencies ("Eff") and spatial resolution ("Res") from analytical models and MC. The predictions of the analytical model (AM column) are derived from the equations of table 2, at the center of the camera in the case of KES ($x = 0$). MC data have been obtained with energy selection $E > 1$ MeV. For the Perfect Detector simulation, the collimator was adjusted to be 100% opaque, and detection with perfect precision and 100% efficiency.

3.2 Prototype Comparison

Performance under clinical conditions is the eventual purpose of these PG cameras, and therefore we here include the results of the clinical case study. Since both cameras prototypes were optimized assuming their particular choice for absorber and energy selection window, here we chose to set

3.2.1 PG profiles

Figure 5.

KES/MPS ratio $\sim 400/350 \sim 0.9$. We can see the impact of the energy selection of the KES prototype (3-6 MeV) that drastically reduces the camera efficiency.

	MPS	KES
Res		
Eff		

Table 6: Detection efficiencies and spatial resolution of MPS and KES prototypes. Energy and TOF selection: $E > 1$ MeV and TOF for MPS – 3-6 MeV and no TOF for KES.

To be completed

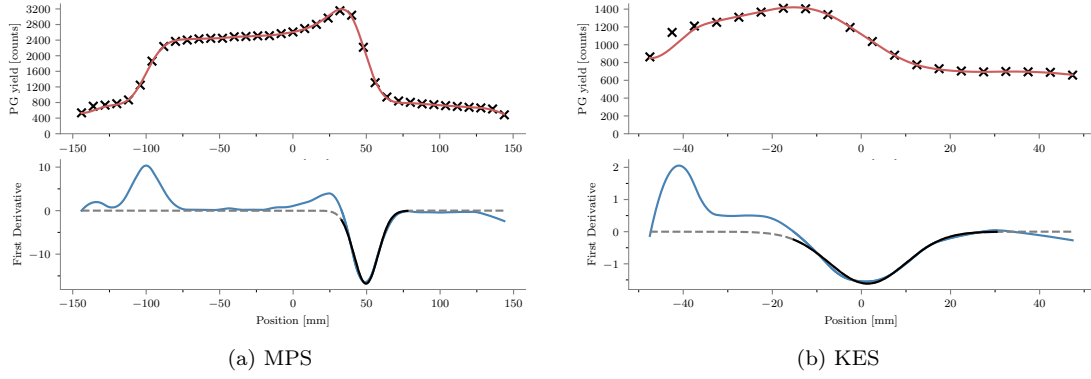


Figure 5: MPS and KES prototypes comparisons. MPS BGO absorber with 1-8 MeV energy selection and TOF selection. KES: LYSO absorber with 3-6 MeV and no TOF selection).

3.2.2 FRP

Figure showing the falloff retrieval precision (FRP) (standard deviation of the falloff position distributions) for the 2 prototypes as a function of the number of incident protons (10^7 , 10^8 , 10^9).

Primaries	Time selection Energy selection Camera	ToF		none		1		3	
		MPS	KES	MPS	KES	MPS	KES	MPS	KES
10^9	AMV perfect det.	0.90	0.10	(no tof or energy selection)					
10^9	detectors as proposed	0.32	0.56	0.36	0.57	0.31	0.60	0.46	0.65
10^8	detectors as proposed	1.05	1.69	1.30	1.96	1.04	1.93	1.34	1.80
10^7	detectors as proposed	2.81	7.96	3.65	12.9	2.96	14.8	19.3	17.1

Table 7: Fall-off retrieval precision (defined as the standard deviation of the FOP over the number of times the simulation is ran. In bold, the cuts and ToF selections as proposed.

4 Discussion

Mention the limitations of the KES: detection efficiency not constant over the FOV.

The discrepancy between the KES efficiencies obtained with the analytical model and MC has still to be understood.

5 Conclusion

6 Acknowledgements

This work was partly supported by SIRIC LYric Grant INCa-DGOS-4664, LABEX PRIMES (ANR-11-LABX-0063 / ANR-11-IDEX-0007) and Fondation ARC. The authors would like to thank Marie-Claude Biston, Thomas Baudier and Gloria Vilches-Freixas for their help finding the CT images and making the treatment plan. We also thank Erik Almhagen and Uppsala University Hospital, Sweden for the treatment plan data presented in this paper.

A Fall-off position and width estimation procedure

A.1 Fall-off position estimation procedure

From a clinical perspective, the range estimate could be more interesting than FOP, because it can distinguish simple offset errors from patient morphological change. While the MPS camera was conceived for whole range PG profile detection, the KES camera FoV was chosen for BP region PG detection only. To make the comparison fair, only the FOP could be considered. Multiple approaches to extracting a FOP from the line profile have been proposed (Gueth et al., 2013; Janssen et al., 2014; Roellinghoff et al., 2014; Smeets et al., 2012; Sterpin et al., 2015). In preparatory work, a number of the proposed procedures were investigated. Significant sensitivity to free parameters on the final FOP estimates were seen. In summary, the FOP estimate depends greatly on the procedure, and often on having yields uncommon on the spot-level in clinical TPs, and also on an absence of unavoidable inhomogeneities.

Therefore the fitting method was not chosen as a topic for study in this paper. Instead, a simple method that works on most the data available to the authors was used: first a smoothed and interpolated spline function is fitted against the detected PG data points, after which a baseline and (distal) peak position are determined. The intersection of the spline with the half-height of the peak above the baseline is then taken as the FOP. A more detailed description of the procedure may be found in appendix A.

1. The measured PG profile is smoothed and interpolated with a smoothing spline function:

$$\sum_{i=1}^n (y_i - \hat{f}(x_i))^2 + \lambda \int_{x_1}^{x_n} \hat{f}''(x)^2 dx \quad (10)$$

where y_i is the measured PG profile and x_i the associated x-coordinates, $\hat{f}(x_i)$ the estimate smoothed spline function and λ a smoothing parameter that determines the penalty for deviating from measurement in exchange for smoothness (second order derivatives are close to zero on smooth functions). $\lambda = 0$ produces a perfect spline fit to the data, while $\lambda \gg 1$ produces a horizontal line. We found that $\lambda = 2$ provided an acceptable trade-off between overfitting to noise and removing too many features, which tends to happen for low statistic measurements.

2. The obtained function is plotted for 1024 x_j , an number that provided a sufficiently high resolution. Any $f(x_j) < 0$ are set to 0.
3. The global maximum is found.
4. The baseline is set equal to the lowest 25% of bins.
5. From the distal end backwards, the first maximum is taken as the distal most peak position, if it is above the threshold of 30% of the difference between baseline and global maximum. If no such point is found, the global maximum is taken as the distal most maximum.
6. The fall-off amplitude (FOA) is set to the difference between the distal maximum and baseline: $FOA = \max - \text{baseline}$. The FOP is obtained by traversing the smoothed profile from the distal end towards the peak until $y_j > \frac{1}{2}FOA$.

The results of this procedure are illustrated in figure 6. Every PG profile was estimated 50 times, and so we obtained 50 estimates for the FOP. It is assumed that the FOPs follow a Gaussian distribution, so the mean of the 50 realizations gives the best FOP estimate and the sigma gives the precision of the ability to estimate the best FOP. Comparing the 50 FOP estimates obtained from the CT with the 50 estimates obtained from the RPCT simulations, gives 2500 possible shift estimates. Again, the distribution of shifts should be centered at the true shift, while the sigma indicates how likely it is that this true shift is detected under the current conditions.

A.2 Fall-off width estimation procedure

Figure 7 shows and illustration of the procedure for two selected profiles obtained with each collimator. To estimate the fall-off with FOW, we smooth the profile in a similar manner as for the FOP estimation, as detailed in appendix A (row 1 in fig. 7). Then, a first and second order derivative is computed. On the first order derivative, a Gaussian is fitted (dashed line on second row), on the interval (solid line) between the profile maximum (Bragg Peak) and the first inflection point past the FOP on the second order derivative (here the 1D PG profile is at the baseline of the background, see third row). The

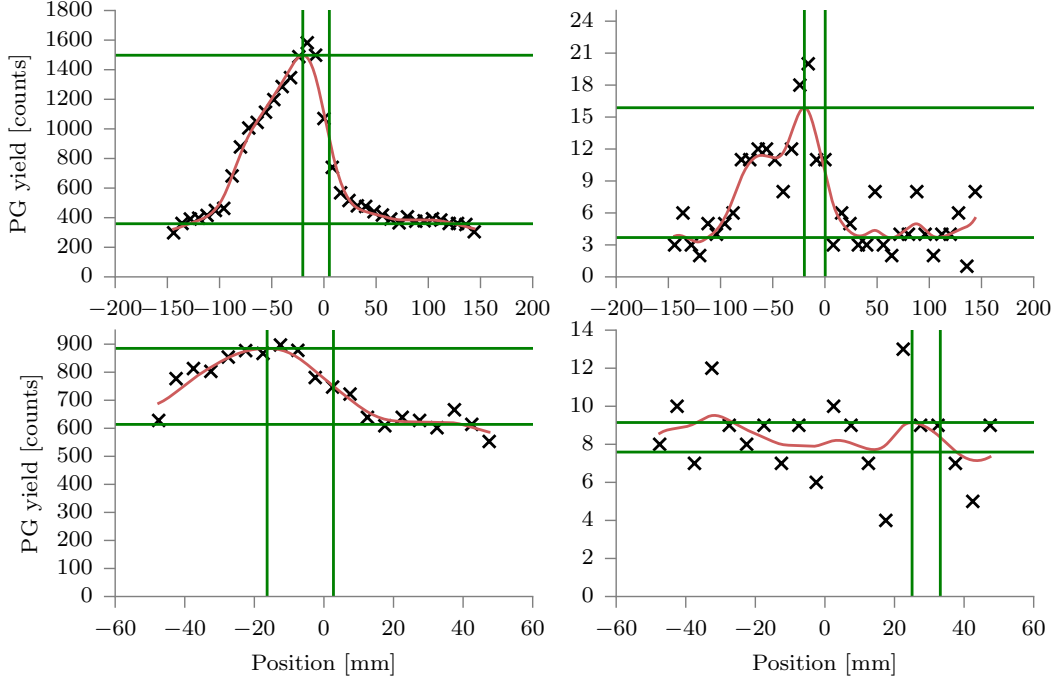


Figure 6: The top row demonstrates the fall-off determination procedure on the multi-parallel camera data; on the bottom row on knife-edge slit camera data. The left column is produced with a PG signal due to 10^9 primaries, while the right column was produced with 10^7 primary protons. In black crosses the measured PG counts are plotted. The smoothed data is shown in red. The green horizontal lines are drawn at the obtained distal maxima and baselines, while the vertical green lines shown the position of the distal maximum and the position of the fall-off. For the bottom-right plot, a history is visible where the procedure fails: the background induces an erroneous peak detection.

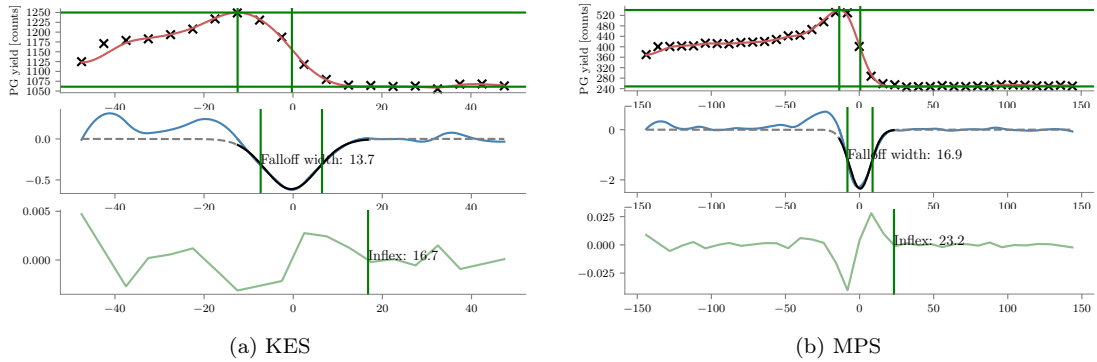


Figure 7: MPS and KES FOW estimation illustrated.

Gaussian is fit with a fixed offset of zero, because the baseline of the background is zero. The full width half max of the fitted Gaussian is then taken as the FOW (second row).

B Verification of the cameras

In [Priegnitz et al. \(2015\)](#) PG shifts due to beam energy shifts are studied for the KES camera: the *detectability* of the fall-off as function of the number of primaries. Here that simulation was recreated: a mono-energetic beam shoots into a waterbox at two energies. 50 realizations are generated with a 139 MeV beam energy, and 50 realizations with 144 MeV. At 10^9 primaries, the distributions are well separated with a shift of 8.3 mm (different from [Priegnitz et al. \(2015\)](#) because of the different material). In figure 13 in [Perali et al. \(2014\)](#) with 10^9 primaries a standard deviation of 1.5 mm is obtained, while here 1.21 and 1.14 mm were obtained. It is sufficient agreement to be confident of our setup and further results.

The KES prototype's sensitivity to accurate positioning with respect to the expected FOP was elaborated upon in [Sterpin et al. \(2015, Section IV.A.3\)](#): the detector response is, due to the KES collimator, not linear as with a parallel slit collimator. In this study, to make the comparison as fair as possible and avoid any bias, alignment on the FOP specific for each spot was ensured as follows: the intermediate PG source image of vpgTLE (equivalent to the PG emission) was projected on the beam axis, and then convolved with a Gaussian of $\sigma = 8.5$ mm, which corresponds to the point spread function (PSF) with a FWHM of 20 mm used in [Priegnitz et al. \(2015\)](#) to approximate the detected profiles from the emitted profile. These profiles will be referred to as "PG + PSF" profiles. As a matter of fact, the MPS prototype has roughly the same PSF as the KES prototype so that "PG + PSF" fall-off position can be considered as the expected position for both cameras.

To verify the implementation of the MPS camera, the precision on the FOP, obtained with the procedure outlined in the previous paragraph, is compared to earlier results. In the caption of figure 9 in [Pinto et al. \(2014\)](#) it is stated that with 10^8 primaries a standard deviation of 1.3 mm is obtained for the detector design used here, which is about 20% different from the results obtained in this study: 1.63 and 1.54 mm.

References

- Christian Golnik, Fernando Hueso-González, Andreas Müller, Peter Dendooven, Wolfgang Enghardt, Fine Fiedler, Thomas Kormoll, Katja Roemer, Johannes Petzoldt, Andreas Wagner, and Guntram Pausch. Range assessment in particle therapy based on prompt γ -ray timing measurements. *Physics in Medicine and Biology*, 59(18):5399–5422, sep 2014. ISSN 0031-9155. doi: 10.1088/0031-9155/59/18/5399. URL <http://stacks.iop.org/0031-9155/59/i=18/a=5399?key=crossref.5437fcd3059992135ec2113679c7dad6>.
- P Gueth, D Dauvergne, N Freud, J M Létang, C Ray, E Testa, and D Sarrut. Machine learning-based patient specific prompt-gamma dose monitoring in proton therapy. *Physics in medicine and biology*, 58(13):4563–77, jul 2013. ISSN 1361-6560. doi: 10.1088/0031-9155/58/13/4563. URL <http://www.ncbi.nlm.nih.gov/pubmed/23771015>.
- Donald L. Gunter. Collimator Design for Nuclear Medicine. *Emission Tomography*, pages 153–168, jan 2004. doi: 10.1016/B978-012744482-6.50011-9. URL <https://www.sciencedirect.com/science/article/pii/B9780127444826500119>.
- Fernando Hueso-González, Fine Fiedler, Christian Golnik, Thomas Kormoll, Guntram Pausch, Johannes Petzoldt, Katja E. Römer, and Wolfgang Enghardt. Compton Camera and Prompt Gamma Ray Timing: Two Methods for In Vivo Range Assessment in Proton Therapy. *Frontiers in Oncology*, 6(April): 1–13, 2016. ISSN 2234-943X. doi: 10.3389/fonc.2016.00080. URL <http://journal.frontiersin.org/article/10.3389/fonc.2016.00080>.
- Brent F B Huisman, J M Létang, É Testa, and D Sarrut. Accelerated Prompt Gamma estimation for clinical Proton Therapy simulations. *Physics in Medicine and Biology*, 61:7725–7743, 2016. ISSN 0031-9155. doi: 10.1088/0031-9155/61/21/7725.
- F M F C Janssen, G Landry, P Cambraia Lopes, G Dedes, J Smeets, D R Schaart, K Parodi, and F Verhaegen. Factors influencing the accuracy of beam range estimation in proton therapy using prompt gamma emission. *Physics in medicine and biology*, 59(15):4427–41, aug 2014. ISSN 1361-6560. doi: 10.1088/0031-9155/59/15/4427. URL <http://www.ncbi.nlm.nih.gov/pubmed/25049223>.
- Antje-Christin Knopf and Antony Lomax. In vivo proton range verification: a review. *Physics in medicine and biology*, 58(15):R131–60, aug 2013. ISSN 1361-6560. doi: 10.1088/0031-9155/58/15/R131. URL <http://www.ncbi.nlm.nih.gov/pubmed/23863203>.
- J. Krimmer, G. Angellier, L. Balleyguier, D. Dauvergne, N. Freud, J. Hérault, J. M. Létang, H. Mathez, M. Pinto, E. Testa, and Y. Zoccarato. A cost-effective monitoring technique in particle therapy via uncollimated prompt gamma peak integration. *Applied Physics Letters*, 110(15):154102, 2017a. ISSN 0003-6951. doi: 10.1063/1.4980103. URL <http://aip.scitation.org/doi/10.1063/1.4980103>.
- J. Krimmer, D. Dauvergne, J.M. Létang, and É. Testa. Prompt-gamma monitoring in hadrontherapy: A review. *Nuclear Instruments and Methods in Physics Research Section A: Accelerators, Spectrometers, Detectors and Associated Equipment*, aug 2017b. ISSN 01689002. doi: 10.1016/j.nima.2017.07.063. URL <http://linkinghub.elsevier.com/retrieve/pii/S0168900217308380>.
- Jochen Krimmer. Development of a Compton camera for medical applications based on silicon strip and scintillation detectors. *Nuclear Instruments and Methods in Physics Research Section A: Accelerators, Spectrometers, Detectors and Associated Equipment*, pages 98–101, 2015.
- Shunsuke Kurosawa, Hidetoshi Kubo, Kazuki Ueno, Shigeto Kabuki, Satoru Iwaki, Michiaki Takahashi, Kojiro Taniue, Naoki Higashi, Kentaro Miuchi, Toru Tanimori, Dogyun Kim, and Jongwon Kim. Prompt gamma detection for range verification in proton therapy. *Current Applied Physics*, 12(2): 364–368, 2012. ISSN 15671739. doi: 10.1016/j.cap.2011.07.027. URL <http://dx.doi.org/10.1016/j.cap.2011.07.027>.
- Yi-Chun Lin, C.Y. Pan, K.J. Chiang, M.C. Yuan, C.H. Chu, Y.W. Tsai, P.K. Teng, C.H. Lin, T.C. Chao, C.C. Lee, C.J. Tung, and A.E. Chen. Monte carlo simulations for angular and spatial distributions in

- therapeutic-energy proton beams. *Radiation Physics and Chemistry*, 140:217 – 224, 2017. ISSN 0969-806X. doi: <https://doi.org/10.1016/j.radphyschem.2017.03.018>. URL <http://www.sciencedirect.com/science/article/pii/S0969806X17302980>. 2nd International Conference on Dosimetry and its Applications (ICDA-2) University of Surrey, Guildford, United Kingdom, 3-8 July 2016.
- Gabriela Llosá, Marco Trovato, John Barrio, Ane Etxebeste, Enrique Muñoz, Carlos Lacasta, Josep F. Oliver, Magdalena Rafecas, Carles Solaz, and Paola Solevi. First Images of a Three-Layer Compton Telescope Prototype for Treatment Monitoring in Hadron Therapy. *Frontiers in Oncology*, 6(February): 14, 2016. ISSN 2234-943X. doi: 10.3389/fonc.2016.00014. URL <http://journal.frontiersin.org/Article/10.3389/fonc.2016.00014/abstract>.
- S D Metzler and R Accorsi. Resolution- versus sensitivity-effective diameter in pinhole collimation: experimental verification. *Physics in Medicine and Biology*, 50(21):5005–5017, nov 2005. ISSN 0031-9155. doi: 10.1088/0031-9155/50/21/004. URL <http://www.ncbi.nlm.nih.gov/pubmed/16237237http://stacks.iop.org/0031-9155/50/i=21/a=004?key=crossref.554d8443522872c9a60e734710db9839>.
- Chul Hee Min, Han Rim Lee, Chan Hyeong Kim, and Se Byeong Lee. Development of array-type prompt gamma measurement system for in vivo range verification in proton therapy. *Medical physics*, 39(4): 2100–7, apr 2012. ISSN 0094-2405. doi: 10.1118/1.3694098. URL <http://www.ncbi.nlm.nih.gov/pubmed/22482631>.
- M Moteabbed, S España, and H Paganetti. Monte Carlo patient study on the comparison of prompt gamma and PET imaging for range verification in proton therapy. *Physics in medicine and biology*, 56(4):1063–82, feb 2011. ISSN 1361-6560. doi: 10.1088/0031-9155/56/4/012. URL <http://www.ncbi.nlm.nih.gov/pubmed/21263174>.
- Harald Paganetti. Range uncertainties in proton therapy and the role of Monte Carlo simulations. *Physics in Medicine and Biology*, 57(11):R99–R117, 2012. ISSN 0031-9155. doi: 10.1088/0031-9155/57/11/R99. URL <http://stacks.iop.org/0031-9155/57/i=11/a=R99?key=crossref.4b6c83cb5125b4a360ead936994fceb4>.
- Seyoun Park, William Plishker, Harry Quon, John Wong, Raj Shekhar, and Junghoon Lee. Deformable registration of CT and cone-beam CT with local intensity matching. *Physics in Medicine and Biology*, 62(3):927–947, feb 2017. ISSN 0031-9155. doi: 10.1088/1361-6560/aa4f6d. URL <http://stacks.iop.org/0031-9155/62/i=3/a=927?key=crossref.6d51a84e851cc257d939edf081764a29>.
- Katia Parodi and Jerimy C. Polf. *In vivo* range verification in particle therapy. *Medical Physics*, 45(11):e1036–e1050, nov 2018. ISSN 0094-2405. doi: 10.1002/mp.12960. URL <https://onlinelibrary.wiley.com/doi/abs/10.1002/mp.12960>.
- G. Pausch, J. Petzoldt, M. Berthel, W. Enghardt, F. Fiedler, C. Golnik, F. Hueso-Gonzalez, R. Lentering, K. Romer, K. Ruhnau, J. Stein, A. Wolf, and T. Kormoll. Scintillator-Based High-Throughput Fast Timing Spectroscopy for Real-Time Range Verification in Particle Therapy. *IEEE Transactions on Nuclear Science*, 63(2):664–672, apr 2016. ISSN 0018-9499. doi: 10.1109/TNS.2016.2527822. URL <http://ieeexplore.ieee.org/document/7454861/>.
- I Perali, a Celani, L Bombelli, C Fiorini, F Camera, E Clementel, S Henrotin, G Janssens, D Prieels, F Roellinghoff, J Smeets, F Stichelbaut, and F Vander Stappen. Prompt gamma imaging of proton pencil beams at clinical dose rate. *Physics in Medicine and Biology*, 59(19):5849–5871, oct 2014. ISSN 0031-9155. doi: 10.1088/0031-9155/59/19/5849. URL <http://stacks.iop.org/0031-9155/59/i=19/a=5849?key=crossref.d1c598721e0b970b36f1c8a6ad1dd1a1>.
- M Pinto, D Dauvergne, N Freud, J Krimmer, J M Letang, C Ray, F Roellinghoff, and E Testa. Design optimisation of a TOF-based collimated camera prototype for online hadrontherapy monitoring. *Physics in medicine and biology*, 59(24):7653–7674, 2014. ISSN 1361-6560. doi: 10.1088/0031-9155/59/24/7653. URL <http://www.ncbi.nlm.nih.gov/pubmed/25415207>.

- Jeremy C Polf, Stephen Avery, Dennis S Mackin, and Sam Beddar. Imaging of prompt gamma rays emitted during delivery of clinical proton beams with a Compton camera: feasibility studies for range verification. *Phys Med Biol*, 60(18):7085–7099, 2015. ISSN 0031-9155. doi: 10.1088/0031-9155/60/18/7085. URL <http://dx.doi.org/10.1088/0031-9155/60/18/7085>.
- M Priegnitz, S Helmbrecht, G Janssens, and I Perali. Measurement of prompt gamma profiles in inhomogeneous targets with a slit camera. *Physics in Medicine and Biology*, 4849:4849, 2015. ISSN 0031-9155. doi: 10.1088/0031-9155/60/12/4849. URL <http://dx.doi.org/10.1088/0031-9155/60/12/4849>.
- Christian Richter, Guntram Pausch, Steffen Barczyk, Marlen Priegnitz, Isabell Keitz, Julia Thiele, Julien Smeets, Francois Vander Stappen, Luca Bombelli, Carlo Fiorini, Lucian Hotoiu, Irene Perali, Damien Prieels, Wolfgang Enghardt, and Michael Baumann. First clinical application of a prompt gamma based in vivo proton range verification system. *Radiotherapy and Oncology*, 118(2):232–237, 2016. ISSN 18790887. doi: 10.1016/j.radonc.2016.01.004. URL <http://linkinghub.elsevier.com/retrieve/pii/S0167814016000074>.
- C Robert, G Dedes, G Battistoni, T T Böhlen, I Buvat, F Cerutti, M P W Chin, a Ferrari, P Gueth, C Kurz, L Lestand, a Mairani, G Montarou, R Nicolini, P G Ortega, K Parodi, Y Prezado, P R Sala, D Sarrut, and E Testa. Distributions of secondary particles in proton and carbon-ion therapy: a comparison between GATE/Geant4 and FLUKA Monte Carlo codes. *Physics in medicine and biology*, 58(9):2879–99, may 2013. ISSN 1361-6560. doi: 10.1088/0031-9155/58/9/2879. URL <http://www.ncbi.nlm.nih.gov/pubmed/23571094>.
- F Roellinghoff, a Benilov, D Dauvergne, G Dedes, N Freud, G Janssens, J Krimmer, J M Létang, M Pinto, D Prieels, C Ray, J Smeets, F Stichelbaut, and E Testa. Real-time proton beam range monitoring by means of prompt-gamma detection with a collimated camera. *Physics in medicine and biology*, 59(5):1327–38, 2014. ISSN 1361-6560. doi: 10.1088/0031-9155/59/5/1327. URL <http://www.ncbi.nlm.nih.gov/pubmed/24556873>.
- David Sarrut, Manuel Bardiès, Nicolas Bousson, Nicolas Freud, Sébastien Jan, Jean-Michel Létang, George Loudos, Lydia Maigne, Sara Marcatili, Thibault Mauxion, Panagiotis Papadimitroulas, Yann Perrot, Uwe Pietrzyk, Charlotte Robert, Dennis R Schaart, Dimitris Visvikis, and Irène Buvat. A review of the use and potential of the GATE Monte Carlo simulation code for radiation therapy and dosimetry applications. *Medical Physics*, 41(6), 2014. doi: <http://dx.doi.org/10.1118/1.4871617>. URL <http://scitation.aip.org/content/aapm/journal/medphys/41/6/10.1118/1.4871617>.
- J Smeets, F Roellinghoff, D Prieels, F Stichelbaut, A Benilov, P Busca, C Fiorini, R Peloso, M Basilavetchia, T Frizzi, J C Dehaes, and A Dubus. Prompt gamma imaging with a slit camera for real-time range control in proton therapy. *Physics in medicine and biology*, 57(11):3371–405, 2012. ISSN 1361-6560. doi: 10.1088/0031-9155/57/11/3371. URL <http://www.ncbi.nlm.nih.gov/pubmed/22572603>.
- Julien Smeets, Frauke Roellinghoff, Guillaume Janssens, Irene Perali, Andrea Celani, Carlo Fiorini, Nicolas Freud, Etienne Testa, and Damien Prieels. Experimental comparison of knife-edge and multi-parallel slit collimators for prompt gamma imaging of proton pencil beams. *Frontiers in Oncology*, 6: 156, 2016. ISSN 2234-943X. doi: 10.3389/fonc.2016.00156. URL <https://www.frontiersin.org/article/10.3389/fonc.2016.00156>.
- Paola Solevi, Enrique Muñoz, Carles Solaz, Marco Trovato, Peter Dendooven, John E Gillam, Carlos Lacasta, Josep F Oliver, Magdalena Rafecas, Irene Torres-Espallardo, Gabriela Llosá, Agostinelli S et Al, Solaz C Barrio J, Etxebeste A, Lacasta C, Muñoz E, Oliver J, Llosá G, Llosá G Cabello J, Etxebeste A, Ziegler S I, Enghardt W et Al, Barrio J Gillam J E, Lacasta C, Torres-Espallardo I, Candela Juan C, Llosá G, Solevi P, Rafecas M, Golnik C et Al, Jan S et Al, Ivanov P Klöckner A, Pinto N, Lee Y, Catanzaro B, Fasih A, Knopf A A, Lomax, Zuber K Kormoll T, Fiedler F, Schöne S, Wüstemann J, Enghardt W, Bruyndonckx P Li Z, Wedrowski M, Vandersteen G, Solaz C Llosá G, Trovato M, Barrio J, Etxebeste A, Munoz E, Lacasta C, Oliver J F, Rafecas M, Solevi P, Llosá G et Al, Llosá G et Al, Thomas D J Marsh J W, Burke M, Meier D et Al, Youn M Y Min C H, Kim C H, Kim J W, Ortega P G et Al, Robertson D Peterson S W, Polf J, Pinto M et Al, Roellinghoff F Pinto M, Dauvergne D, Freud N, Krimmer J, Letang J M, Ray C, Testa E, Mackin D S Polf J C, Avery S, Beddar S, Polf J C et Al, Robert C et Al, Schumann A Rohling H, Golnik C, Enghardt W, Hueso-González

- F, Kormoll T, Pausch G, Fiedler F, Elsässer T, Schardt D, Schulz-Ertner D, Roemer K, Schumann A, Petzoldt J, Dendooven P, Enghardt W, Golnik C, Hueso-González F, Kormoll T, Pausch G, Fiedler F, Priegnitz M, Shakirin G, Braess H, Fiedler F, Kunath D, Laube K, Parodi K, Enghardt W, Smeets J et al, Trovato M, Stankova V, Barrio J, Gillam J E, Lacasta C, Rafecas M, Solaz C, Llosá G, Bortfeld T, Verburg J M, Riley K, Seco J, Xu D Z, and He. Performance of MACACO Compton telescope for ion-beam therapy monitoring: first test with proton beams. *Physics in Medicine and Biology*, 61(14): 5149–5165, 2016. ISSN 0031-9155. doi: 10.1088/0031-9155/61/14/5149. URL <http://stacks.iop.org/0031-9155/61/i=14/a=5149?key=crossref.6bf836448c34a4bc8348edeba28d35c4>.
- E Sterpin, G Janssens, J Smeets, François Vander Stappen, D Prieels, Marlen Priegnitz, Irene Perali, and S Vynckier. Analytical computation of prompt gamma ray emission and detection for proton range verification. *Physics in Medicine and Biology*, 60(12):4915–4946, 2015. ISSN 0031-9155. doi: 10.1088/0031-9155/60/12/4915. URL <http://stacks.iop.org/0031-9155/60/i=12/a=4915?key=crossref.aabd8815e135401a22d165e343a7bac4>.
- E. Testa, M. Bajard, M. Chevallier, D. Dauvergne, F. Le Foulher, N. Freud, J. M. Letang, J. C. Poizat, C. Ray, and M. Testa. Monitoring the Bragg peak location of 73 MeV carbon ions by means of prompt γ -ray measurements. *Applied Physics Letters*, 93(9):1–10, 2008. ISSN 00036951. doi: 10.1063/1.2975841. URL <http://arxiv.org/abs/0809.0185><http://dx.doi.org/10.1063/1.2975841>.
- P.G. Thirolf, S. Aldawood, M. Böhmer, J. Bortfeldt, I. Castelhana, G. Dedes, F. Fiedler, R. Gernhäuser, C. Golnik, S. Helmbrecht, F. Hueso-González, H. v.d. Kolff, T. Kormoll, C. Lang, S. Liprandi, R. Lutter, T. Marinšek, L. Maier, G. Pausch, J. Petzoldt, K. Römer, D. Schaart, and K. Parodi. A Compton camera prototype for prompt gamma medical imaging. *EPJ Web of Conferences*, 117:05005, 2016. ISSN 2100-014X. doi: 10.1051/epjconf/201611705005. URL <http://www.epj-conferences.org/10.1051/epjconf/201611705005>.